ELSEVIER

Contents lists available at ScienceDirect

Materials and Design

journal homepage: www.elsevier.com/locate/matdes



Meso-scale modeling of multiple-layer fabrication process in Selective Electron Beam Melting: Inter-layer/track voids formation



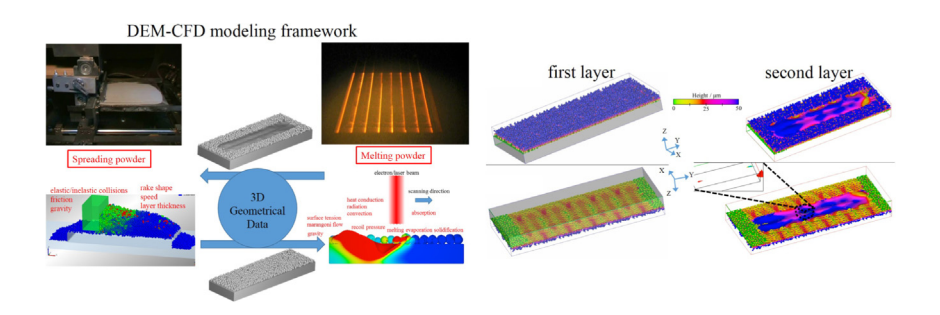
Wentao Yan^a, Ya Qian^b, Wenjun Ge^c, Stephen Lin^a, Wing Kam Liu^a, Feng Lin^b, Gregory J. Wagner^{a,*}

- ^a Department of Mechanical Engineering, Northwestern University, Evanston, IL 60201, United States
- ^b Department of Mechanical Engineering, Tsinghua University, Beijing 100084, PR China
- ^c Department of Mechanical Engineering, Korea Advanced Institute of Science and Technology (KAIST), Daejeon, Republic of Korea

HIGHLIGHTS

- An integrated DEM-CFD modeling framework to simulate the powder being spread and then melted.
- Meso-scale simulations of SEBM processes of multiple-layer multipletrack along various scan paths.
- The formation of inter-layer/track voids due to lack of fusion and the influence of scan path.

GRAPHICAL ABSTRACT



ARTICLE INFO

Article history:
Received 31 October 2017
Received in revised form 1 December 2017
Accepted 16 December 2017
Available online 22 December 2017

Keywords: Electron beam Additive manufacturing Thermal-fluid flow Discrete element method Multiple layers Scan path

ABSTRACT

Selective Electron Beam Melting (SEBM) is a promising powder-based metallic Additive Manufacturing (AM) technology. However, most powder-scale modeling efforts are limited to single track process, while it is also difficult to experimentally observe the interaction between tracks and layers. In this study, we develop an integrated modeling framework to investigate the SEBM process of multiple tracks and multiple layers. This approach consists of a Discrete Element model of powder spreading and a Computational Fluid Dynamics (CFD) model of powder melting. These two models exchange 3D geometrical data as a cycle to reproduce the manufacturing process of multiple tracks along various scan paths in multiple powder layers. This integrated modeling approach enables further understanding of how current tracks and layers interact with previous ones leading to inter-track/layer voids. It also incorporates more influential factors, particularly the layerwise scan strategy. The inter-layer/track voids due to the lack of fusion are systematically discussed in light of our simulation results which qualitatively agree with experimental observations in literature.

© 2017 Elsevier Ltd. All rights reserved.

1. Introduction

Powder bed based Additive Manufacturing (AM) technologies for metallic components, including Selective Laser Melting (SLM) and Selective Electron Beam Melting (SEBM), have drawn increasing attention over the past decade. In addition to manufacturing

Corresponding author.

E-mail address: gregory.wagner@northwestern.edu (G.J. Wagner).

components with complex geometry, these powder-based AM technologies are opening new avenues for locally manipulating chemical compositions and mechanical properties. For example, Ge et al. [1–3] manufactured functionally graded Ti-TiAl materials using SEBM.

The SLM/SEBM process mainly consists of two repeated procedures [1], as shown in Fig. 1.

- 1. Apply one layer of powder on a preheated platform or previously deposited layers.
- 2. Selectively melt the powder bed along the designated scan path.

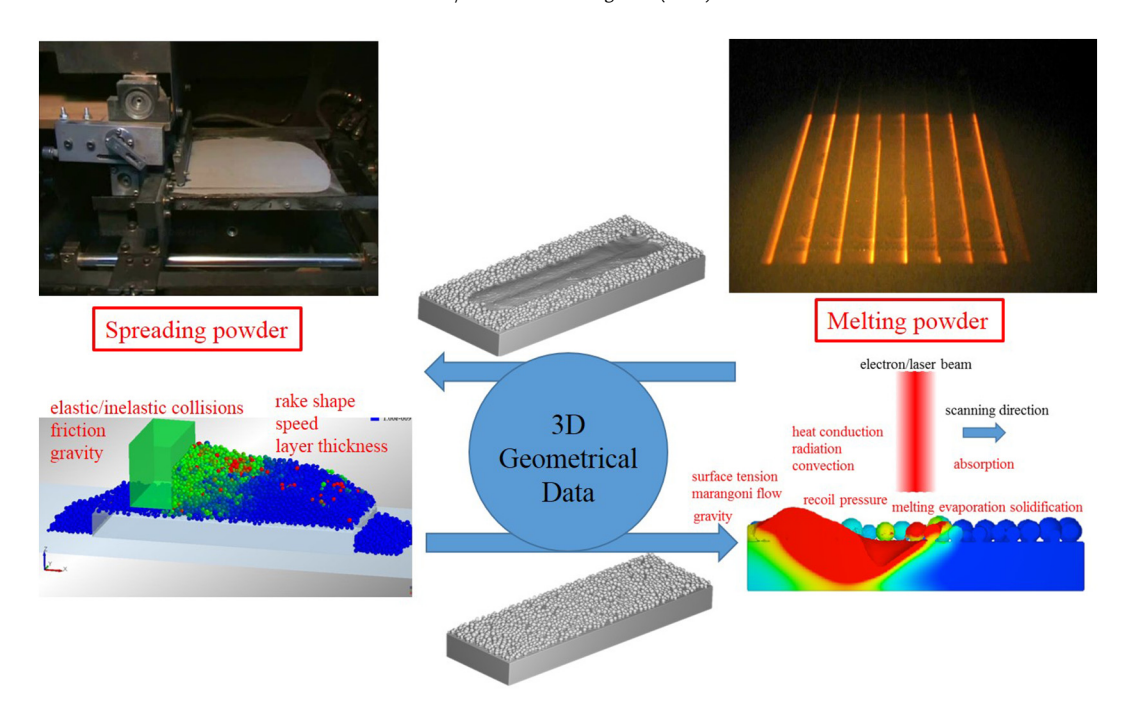


Fig. 1. Integrated modeling framework to reproduce the major procedures of SEBM.

Although the basic principle of SLM/SEBM is rather straightforward, the actual processes consists of multiple physical phenomena, e.g., powder particle packing, heat transfer, phase transformation and fluid flow, where a number of factors have large influence over the process and fabrication quality [4]. There are a considerable number of fundamental physical mechanisms affecting each fabrication procedure, complicating understanding of the process. For example, some previous studies proposed different and even conflicting explanations for the formation of defects, such as the balling effect [5,6]. The uncertainty of fabrication quality is considered to be a serious barrier to be a wider adoption of AM technologies in industry [7]. Moreover, the selection of optimal process parameters mostly depends on trial-and-error experiments, which are low-efficiency and expensive. While the physical process is challenging to measure experimentally, numerical modeling is a powerful tool to assess the physical mechanisms and the influence of numerous fabrication parameters, and finally guide optimal param-

Several meso-scale models have been developed to investigate the melting process of the randomly distributed powder particles in the powder bed [8-10]. Körner et al. [8,11] employed the 2-D Lattice Boltzmann Method (LBM) to model the powder melting process in SEBM, with a rain drop model to generate each powder layer. Since the rain drop model does not fully incorporate the mechanical interactions between particles and the rake, the relative density of the generated powder bed is higher than that in reality [8]. Ammer et al. [12] extended the LBM model to the 3-D case. Khairallah et al. [9] developed a meso-scopic model for SLM to investigate the formation mechanism of pores, spatter and denudation in single track formation process using the ALE3D multi-physics code. Qiu et al. [13] used the open-source code OpenFOAM to simulate the melt pool flow in the SLM process to study the surface structure and porosity development. These models incorporate the most important forces driving the molten pool flow, including surface tension, the Marangoni effect, and recoil pressure. The Discrete Element Method (DEM) has also been used to simulate the particle sintering process, incorporating heat transfer but not molten pool flow [14–18].

Most powder melting models only simulate the melting process of a single track, which has not shed light into how successive tracks and layers interact with each other. Moreover, few studies have been done to comprehensively incorporate the procedure of powder spreading.

In this study, we develop an integrated modeling framework to simulate the two repeated procedures of SEBM: spreading the powder layer and selectively melting the newly applied powder. This approach consists of a powder spreading model using the DEM and a thermal-fluid flow model for powder melting, as shown in Fig. 1. The powder spreading model simulates the frictional contact and collisions both between particles and with the rake and substrate, and the powder melting model captures the material evolution process as a result of input energy, including heat transfer, phase change, and molten pool flow. The 3D geometry model of the powder bed used in the powder melting model is generated by the powder spreading model, with the powder size distribution taken from experimental measurements. After simulating the melting and solidification process, the solidified geometry is transferred back to the powder spreading model to apply a fresh powder layer. These two simulations are repeated to reproduce a typical multiple-layer, multiple-track manufacturing process. Based on this, we study how the current layer and track interact with previous ones, and particularly how inter-layer/track voids are formed. Various scan paths are investigated to assess the influence on the inter-layer/track voids, thereby providing valuable guidance for the optimization of scan paths. The simulation results qualitatively agree with experimental observations in literature.

2. Modeling of powder spreading process

We perform 3D DEM simulations of a rake being pushed over a powder bed, as shown in Fig. 2. This model consists of (1) a translating rake with a designated shape, (2) a substrate (flat surface) or previous layers (fluctuating surface), (3) a vertical wall which corresponds to lowering the plate in one layer thickness, and

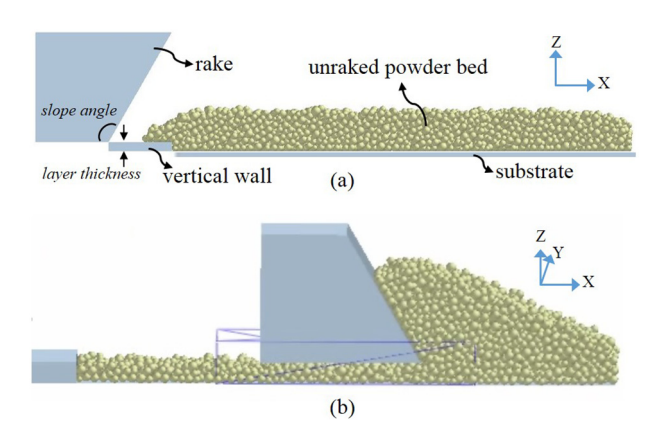


Fig. 2. (a) Initial configuration of powder spreading simulation, with a rake angle greater than 90° . (b) Intermediate position of powder spreading simulation, with a rake angle less than 90° .

(4) spherical powder particles with diameters ranging in a normal distribution with D10 = $30 \,\mu m$ and D90 = $50 \,\mu m$. In Fig. 2, rakes with two different slope angles are shown to emphasize the ability to investigate the influence of rake shape.

Spherical powder particles are initially introduced onto the plate by allowing them to fall under gravity to form a powder bed covering the substrate with a varying thickness. The rake then moves from left to right to spread the powder. Vibration effects of the rake system are not considered in our current model.

In this process, the powder particle motion is governed by the frictional contact interaction and body force. The Hertz-Mindlin model is used to model contact interactions [19]. For the interaction between two contact particles with radii of R_1 and R_2 and masses of m_1 and m_2 , the contact forces in the normal and tangential directions consist of nonlinear deformation and damping.

$$\vec{F_n} = \left(-K_n |\delta_n|^{3/2} - \gamma_n |\dot{\delta_n}| \right) \vec{e_n} \tag{1}$$

$$\vec{F}_t = -\left(K_t|\xi_t| + \gamma_t|\dot{\xi}_t|\right)\vec{e}_t \tag{2}$$

where $\overrightarrow{e_n}$ and $\overrightarrow{e_t}$ are the unit vectors in the normal and tangential (along the relative velocity) directions, $|\delta_n|$ and $|\delta_n|$ are the relative displacement and velocity in the normal direction, $|\xi_t|$ and $|\xi_t|$ are the relative displacement and velocity in the tangential direction, K_n and γ_n are the effective stiffness and damping coefficient in the normal direction, and K_t and γ_t are the effective stiffness and damping coefficient in the tangential direction:

$$\begin{cases} K_{n} = \frac{2E}{3(1-v^{2})} \sqrt{\frac{R_{1}R_{2}}{R_{1}+R_{2}}} \\ K_{t} = \frac{2E}{(2+v)(1-v)} \sqrt{\frac{R_{1}R_{2}}{R_{1}+R_{2}}} \delta_{n} \\ \gamma_{n} = -\sqrt{\frac{5}{6}} \cdot \frac{\ln(\theta)}{\sqrt{\ln^{2}(\theta)+\pi^{2}}} \cdot \sqrt{3K_{n} \frac{m_{1}m_{2}}{m_{1}+m_{2}}} \\ \gamma_{t} = -\sqrt{\frac{5}{6}} \cdot \frac{\ln(\theta)}{\sqrt{\ln^{2}(\theta)+\pi^{2}}} \cdot \sqrt{2K_{t} \frac{m_{1}m_{2}}{m_{1}+m_{2}}} \end{cases}$$
(3)

where E, v and θ are the Young's modulus, Poisson's ratio and restitution coefficient. The material parameters of Ti-6Al-4 V used in the simulation are listed in Table 1.

If $|E_t|\xi_t| + \gamma_t \dot{\xi_t}| > \mu_f |F_n|$, tangential sliding will occur. In this case, the tangential force is the maximum friction, and is given as

$$\vec{F_t} = -\mu_f |F_n| \vec{e_t} \tag{4}$$

Table 1Material parameters of Ti-6Al-4 V [6].

Property	Value
Density (ρ)	4000 kg/m ³
Young's modulus (E)	124 GPa
Poisson ration (v)	0.41
Sliding friction coefficient (μ_f)	0.5
Restitution coefficient (θ)	0.5
Surface energy density (Ψ)	0.0002 J/m ²
Solidus temperature (T_s)	1878 K
Liquidus temperature (T_l)	1928 K
Latent heat of melting (L_m)	$2.86 \times 10^{5} \text{ J/kg}$
Latent heat of evaporation (L_{ν})	$9.7 \times 10^{6} \text{ J/kg}$
Saturated vapor pressure (P_{s0}) at $T_0 = 3315$ K	$1.013 \times 10^5 \text{ Pa}$
Specific heat (c)	872 J/(K•kg)
Thermal conductivity at solidus state (k)	16 W/(m•K)
Thermal conductivity at liquidus state (k)	32 W/(m•K)
Surface radiation coefficient (α_b)	0.4
Surface tension coefficient (σ)	1.68 N/m
Temperature sensitivity of surface tension coefficient (σ_s^T)	0.00026
Viscosity (μ)	0.005 Pa•s

In addition to the contact repulsive force, the cohesive nature of fine particles leads to an attractive force. Here we use the JKR cohesion model [20] that was originally implemented to incorporate the van der Waals forces between fine and dry particles

$$\overrightarrow{F_{JKR}} = 4\sqrt{\frac{\pi a^3 \Psi E}{2(1 - \upsilon^2)}} \overrightarrow{e_t}$$
 (5)

where the cohesion force is mainly determined by the surface energy density (Ψ) of the material and the radius of the contact area (a).

The commercial software EDEM v2.7 is used to perform the powder bed spreading simulations. To ensure stability, the Rayleigh time-step limit is employed:

$$\Delta t < \frac{\pi R_{\min} \sqrt{\rho/E}}{0.163 \upsilon + 0.877} \tag{6}$$

The physical meaning of the time-step limit is the time for a shear wave to propagate through a solid particle. In order to ensure a tractable time-step size, the small number of very fine particles (diameter below $30\,\mu m$) measured in experiments are excluded in the model, while the influence of these fine particles on the relative packing density can be neglected.

A variety of factors, including but not limited to the powder size distribution, the layer thickness, and the rake shape and its translational speed, can be incorporated in the model. This enables a link between the machine configuration and the manufacturing process. However, detailed investigation of powder spreading is out of the scope of this study, and we merely employ the DEM simulation to generate the powder bed, which has a relative density around 50% as measured in experiments [21].

3. Modeling of powder melting process

The thermal-fluid flow model simulates the packed powder particles being heated by a moving electron beam, and then melting, flowing, and finally solidifying into dense parts. This highly transient evolution process is governed by mass, momentum and energy conservation. Details of the governing equations and numerical implementations can be found in our previous paper [22]. In brief, the surface tension force, Marangoni effect, recoil pressure, buoyancy and gravity are incorporated in the molten pool flow; the input heat source model, latent heat, heat conduction, surface radiation and evaporative heat loss are incorporated in the energy conservation equation and its boundary conditions; evaporative mass loss is also

incorporated based on the formulation in [23], which is minor in this simulation case. The heat source model for an electron beam is established based on Monte Carlo simulations of electron-atom interactions [24,25], and it is applied to the materials by tracing the penetration of numerous smaller sub-beams. The penetration of each sub-beam starts from the free surface, which is captured using the Volume of Fluid (VOF) method.

In the SEBM process, a pre-heating step is typically included after spreading the powder and before the selective melting to avoid the "powder splash" effect [26]. Our model does not explicitly include pre-sintering of the particle, but approximates this step by applying a uniform pre-heating temperature as an initial condition for each layer.

The commercial software FLOW-3D v10.1 [27] is used to perform the simulations, in which a structural Eulerian mesh with a cell size of 5 µm is used. In this study, the layer thickness is 0.05 mm, and the electron beam power and scan speed are fixed at 60 W and 0.5 m/s. This set of manufacturing parameters is in the thermalconduction mode, consistent with the physical SEBM process in which the keyhole mode is avoided in order to reduce porosity due to entrapped gas. Different sets of parameters in the thermalconduction mode were studied in our previous work [22], showing very similar molten pool behaviors, because the driving forces are very similar across a range of process parameters. Thus, this set of manufacturing parameters can qualitatively illustrate the fundamental mechanisms. In a typical simulation case in this study, the number of computational cells is about 7 million, the physical time is about 16 ms, and the computation time on a common desktop with an Intel Core i7-2600 CPU is about 700 h. A mesh convergence test has been performed for the model to confirm that mesh-sensitivity effects can be neglected. The powder and substrate material is Ti-6Al-4V, and the material parameters are listed in Table 1. It should be noted that material parameters are treated as constants due to the lack of reliable temperature-dependent material parameters.

To model the manufacturing process of multiple layers, after the simulation of the first layer is complete, the detailed solidified shape is transferred into the DEM model in the form of an STL file. After applying a new powder layer on the solidified tracks, the geometry information is transferred back to the thermal-fluid flow model, again in an STL file.

4. Results and discussion

4.1. Multiple layers of single track: thin-wall structures

Through the integrated modeling framework, we can model the manufacturing process of multiple powder layers. One of the simplest manufacturing cases is that of depositing one single track layer by layer, which is often used to build thin-wall and cellular structures. After melting one track in a powder layer, the next powder layer is applied and spread. The scan direction of the single track in the newly applied layer can be the same as or opposite that in the previous layer (see Fig. 3 (a) and (d)). In the simulation results colored by fused zone, the red regions represent the regions that have been melted and then solidified, and the blue regions represent the unmelted regions; regions that are between blue and red denote locations that at some instant exceed the solidus but never the liquidus temperature.

The melted width of a single track in the first layer is around $240\,\mu m$. However, during the melting of the second layer, the remelted zone within the first layer is narrower, varying between $170\,\mu m$ and $210\,\mu m$. The remelted width determines the effective thickness of the thin-wall structure, since it determines the effective width of the single track as demonstrated in our previous paper [22]. As the track is higher along the central line of the scan track, and lower near the boundaries of the track, the powder layer to be melted

has a larger thickness near the track boundaries than the designated layer thickness, as shown in Fig. 4 (a1) and (a2). More importantly, the power intensity is lower near the boundaries. Thus, the boundary regions of the previous single track are less likely to be remelted. Similarly, the melt depth varies along the scan direction (see Fig. 3 (c) and (f)), because of the height fluctuation of the first track and the resultant inconsistencies of the second powder layer.

It should be noted that inter-layer voids are formed in the beginning of the scan in both cases (see the dashed black ellipsoids in Fig. 3 (f) and Fig. 4 (b1)). Near the start of each track, the melted depth is not as large as it is later in the track, since there has been no heat accumulation in the starting region. This is similar to the multi-track case demonstrated in [22]. These defects have been experimentally observed [28] as shown in Fig. 5 (c). From our combined experimental and computational observation, we hypothesize that it is better to scan the edge first and then scan the inner section, which is called a "contouring" scan strategy [29,30]. By using the strategy, we can ensure that the starting regions are melted and consolidated, reducing the number of voids near the edges of the part. This also has been experimentally demonstrated by Tammas-Williams et al. [30].

The results of these two cases can be compared with the single track in a single layer with a thickness of 0.1 mm (see Fig. 4 (d) and Fig. 3 (g)), which is twice the thickness of each individual layer in our two-layer simulations. There are more voids in the starting region of the single track manufactured in a 0.1 mm-thick powder layer, and the height fluctuation is more pronounced. Thus, manufacturing in two thinner layers is usually beneficial to product quality at a cost of a longer production time.

4.2. Multiple layers of multiple tracks

Simulations of multiple tracks in a single powder layer have been reported in our previous paper [22]. Here we present simulations of multiple layers of multiple tracks, which more closely resembles the manufacturing process of complex structures. A second powder layer is spread on the solidified Z-shaped tracks (adjacent tracks in the same direction), and then another two tracks are manufactured along Z-shaped scan, along the same or opposite direction as the corresponding tracks in the first layer, as shown in Fig. 6. These cases are referred to as "2-layer-2-track." It is assumed that additional layers or tracks will result in a repeated pattern similar to how the second layer or track interacts with the first layer or track. Thus, for this study, "2-layer-2-track" cases are considered sufficient to investigate the interactions between tracks and layers.

In the unidirectional "2-layer-2-track" case (see Fig. 6 (a)), a void is observed at $x=1.83 \, \text{mm}$ and $y=0.493 \, \text{mm}$, which is near the middle of the two scan paths. The mechanism for the defect is the following: in this region, the melt depth is relatively small, since it is far from the focal center of the electron beam, resulting in a weaker energy intensity; additionally, the actual powder layer is thicker at this point because the fused surface in the middle region between the centers of the two tracks is the lowest in the first layer.

In the counter-directional "2-layer-2-track" case (see Fig. 6 (b)), the void is no longer observed in the same spot as that of the previous case. However, a void is observed at x=1.82~mm and y=0.488~mm, about 15 μm from that. The minor difference may probably be due to the molten flow which is influenced by local configurations of powder particles. Additionally, a cluster of voids are observed near the start of the tracks in the second layer (see Fig. 6 (b3)). The mechanism for the defect is the following: as discussed, the melt depth near the start is not as large as it is farther along the track, while the actual powder layer is thicker, since the track height of previous layer is lower. Thus, the voids near the edge are more pronounced in counter-directional cases than in uni-directional. The

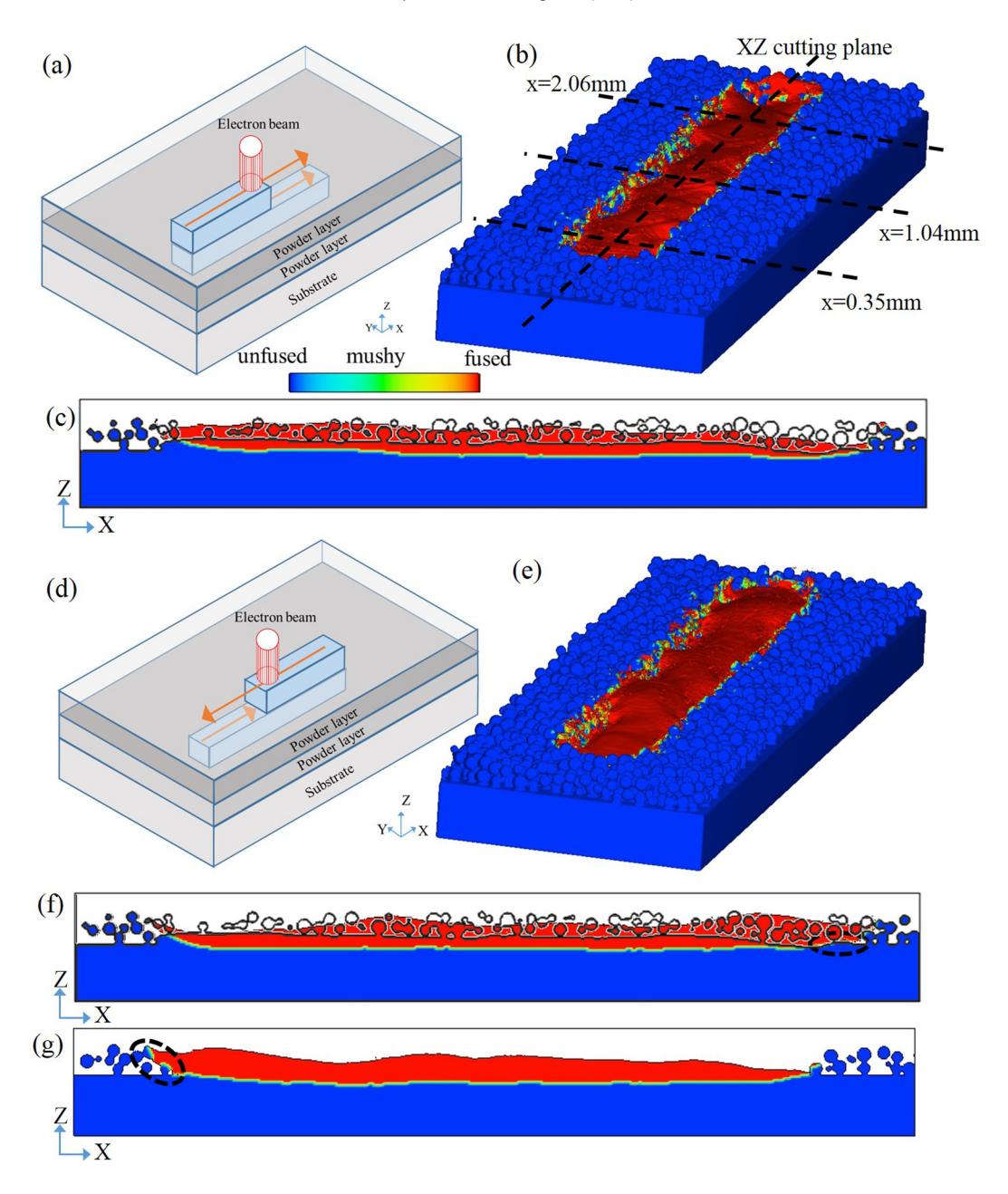


Fig. 3. Simulations of multiple layers of single tracks. The scan direction of the single track in the second layer can be the same as (a–c) or opposite (d–f) that of the first layer. The schematic, 3D view and XZ cross section view for the two cases are in (a–c) and (d–f), respectively. The layer thickness is 0.05 mm. In (c) and (f), the outlines represent the configuration of first layer fused zone and the powder particles before scanning the second layer. (g) The same XZ cross section view for the single track in a 0.1 mm-thick layer for comparison.

voids near the edges of the part in both simulation cases agree with previous experimental observation [28], as shown in Fig. 5 (c).

Because of the consolidate of the inter-particle voids during melting, the fused surface of the first powder layer is lower than the height of the original powder layer (0.05 mm). Therefore, after spreading the second powder layer, the actual thickness of the new powder layer varies between 0.05 mm and 0.1 mm (even though the substrate is lowered only by 0.05 mm). This thickness change can explain some experimental observation of the manufacturing quality becoming worse after the first several layers. Therefore, in order to ensure sufficient quality of the following layer, the energy input parameters, such as power and scan speed, should be selected such that the input energy can melt a powder layer of more than twice the designated layer thickness, considering the relative packing density

of around 50% for the powder bed and allowing for inconsistencies in the powder layer thickness.

4.3. Influence of layer-wise scan strategy

The layer-wise scan strategy has been proved to be critical to the as-built quality, including densification, micro-structure, and residual stress [31]. In this study, we investigate two types of layerwise scan strategy (see Fig. 7): (1) layer-wise rotated by an angle θ (0° $\leq \theta \leq$ 180°), and (2) parallel and interlaced in either the same or opposite direction.

The two cases studied in Section 4.2 are examples of layer-wise rotated scan with $\theta=0^\circ$ and $\theta=180^\circ$, respectively. The cases of layer-wise rotated scan with $\theta=90^\circ$ and $\theta=45^\circ$ are also simulated,

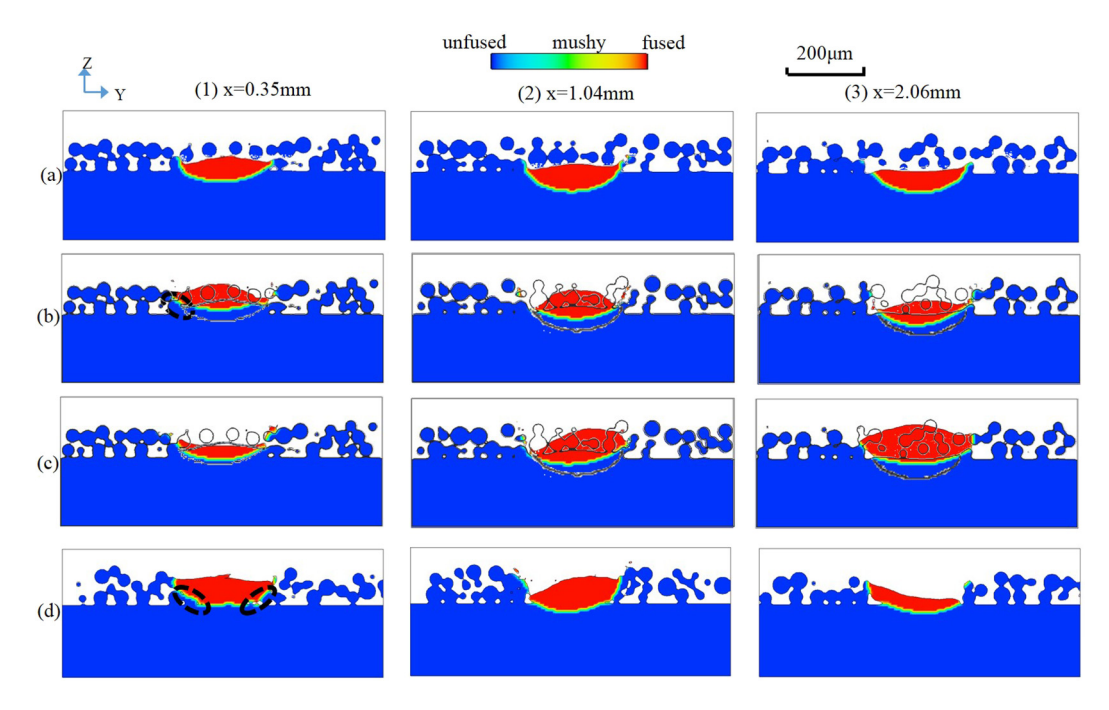


Fig. 4. The 2-layer-1-track case: the fused zone of (a) the single track in the first 0.05 mm-thick layer, and (b) the single track in the second 0.05 mm-thick layer along the same scan direction as the first layer, and (c) the scan direction in the second layer is opposite that of the first layer. (d) *The single track in a 0.1mm-thick layer.* In (b) and (c), the outlines represent the configuration of the first layer fused zone and the powder particles before scanning the second layer (i.e. (a)). Cross-section views are taken at (1) x = 0.35 mm, (2) x = 1.04 mm, and (3) x = 2.06 mm, as shown in Fig. 3 (b). The sub-figures are referred according to their relative positions, such as "a1" for the top left one.

as shown in Figs. 8 and 9. Voids are observed in both configurations. These voids are located at positions that are midway between scan centerlines in both the first and second layers (see the red dots in Fig. 7 (a)). These locations are least likely to be fully fused, for reasons previously discussed in Section 4.2. Such locations exist for any value of θ , but are most prevalent for $\theta=0^\circ$ and $\theta=180^\circ$.

The layer-wise interlaced scan strategy is observed to be more beneficial for reducing the porosity in as-built products than the layer-wise rotated scan strategy. No voids are observed, as shown in Fig. 10. The scan lines in the second layer lie in the middle of the scan lines in the first layer, eliminating the void formation midway between scan centerlines.

4.4. Voids

The size and spatial distribution of voids are found to be remarkably influenced by the scan strategy. Most voids are observed midway between the centerlines of adjacent scan paths in both layers, as discussed in Section 4.3. Because the voids are due to lack of fusion, the size is proportional to the powder size distribution and the difference between the hatching distance and melting

width. The size of the unfused region between two tracks equals the difference between the hatching distance and the melt width. If the original inter-particle voids are smaller than the unfused region, the resulting void size is unchanged and is a function of initial powder size distribution. Conversely, if the inter-particle voids are partially filled, the resultant void size is mainly determined by the difference between the hatching distance and melting width. In the simulations presented in this paper, with a power of 60 W and a scan speed of 0.5 m/s, the effective melting width of the second powder layer ranges between 195 μm and 235 μm , where the fluctuation is caused by the fluctuation of powder layer thickness ranging between 50 μm and 100 μm . Therefore, the void size perpendicular to the scan direction is around 5 μm (hatching distance 200 μm minus smallest melting width 195 μm), while the size along the scan direction could be larger (see Figs. 6 and 8).

However, it is noted that randomness exists because of variability in powder packing arrangement. Statistically, the randomness has been proven to be minor by experimental measurement [30]. Therefore, it is wise to employ experimentally-measured statistical properties to quantitatively validate the meso-scale models. For instance, the size distribution of voids and the overall porosity in

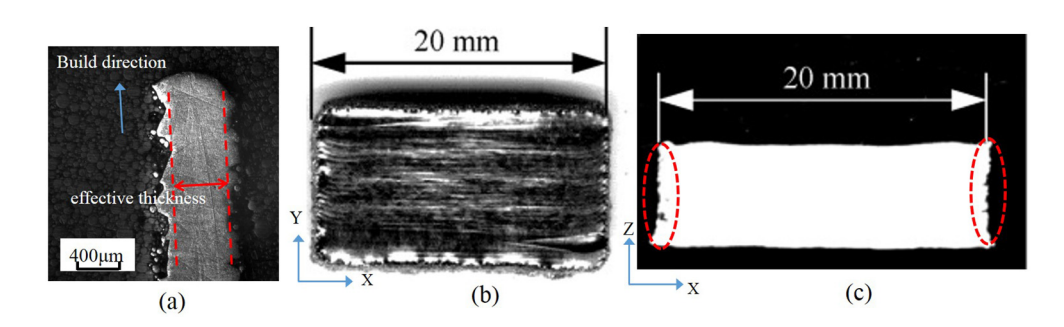


Fig. 5. Experimental observations: (a) cross section of the thin-wall structure, (b) outer side surface of a cubic specimen and (c) cross section of the cubic specimen along its build direction [28].

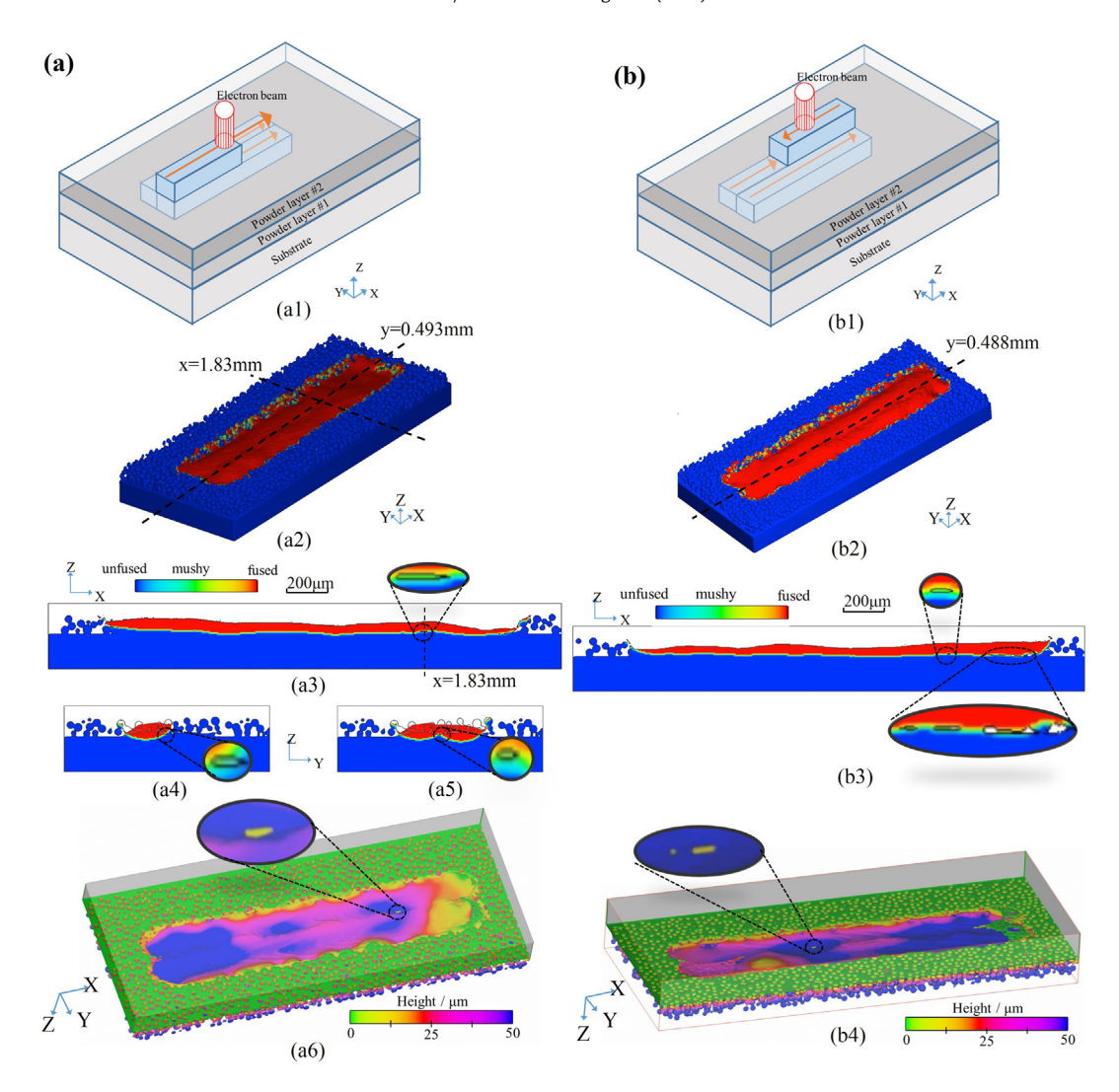


Fig. 6. (a) Unidirectional "2-layer-2-track" case: (a1) Schematic, (a2) 3D view of the simulation result colored by fusion, (a3) XZ cross section view at y = 0.493 mm, (a4) (a5) YZ cross section view at the x = 1.83 mm, after the first and second track of the second layer, respectively, and (a6) 3D view of the free surfaces, *viewed from below (the -z direction)* and colored by the height from the substrate surface to show the voids clearly. (b) Counter-directional "2-layer-2-track" case: (b1) Schematic, (b2) 3D view of simulation result, (b3) XZ cross section view at y = 0.488 mm, and (b4) 3D view of the free surfaces, *viewed from below (the -z direction)* and colored by the height from the substrate surface to show the voids clearly.

the as-built product are reasonable indices to use to validate the prediction of powder melting models, while the relative packing density is a good index to validate powder spreading models.

Moreover, it should be mentioned that the observed voids in this study are due to the lack of fusion between tracks and layer. There is

another different type of void, which is caused by trapped gas [30]. The gas may come from evaporation and entrainment (particularly in keyhole mode [32]), inner pores of the virgin powder particles, or contamination. The current model is not able to capture this type of void, making it difficult to quantitatively compare simulation results

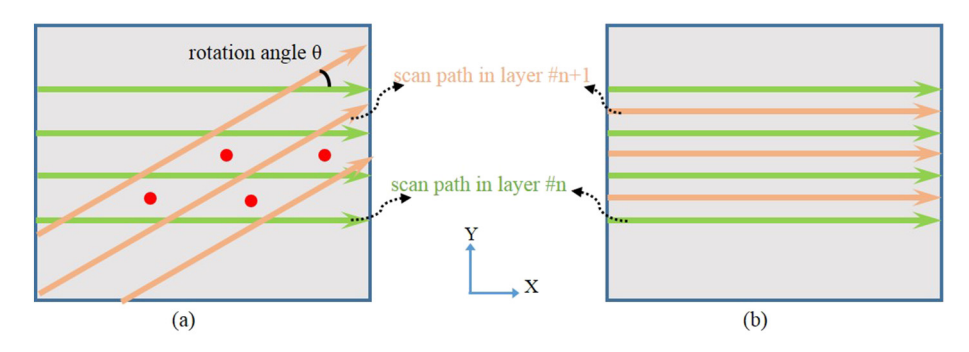


Fig. 7. Schematic of layer-wise scan strategy. (a) Layer-wise rotated for θ , and (b) parallel and interlaced scan. The red dots are possible locations where voids may form.

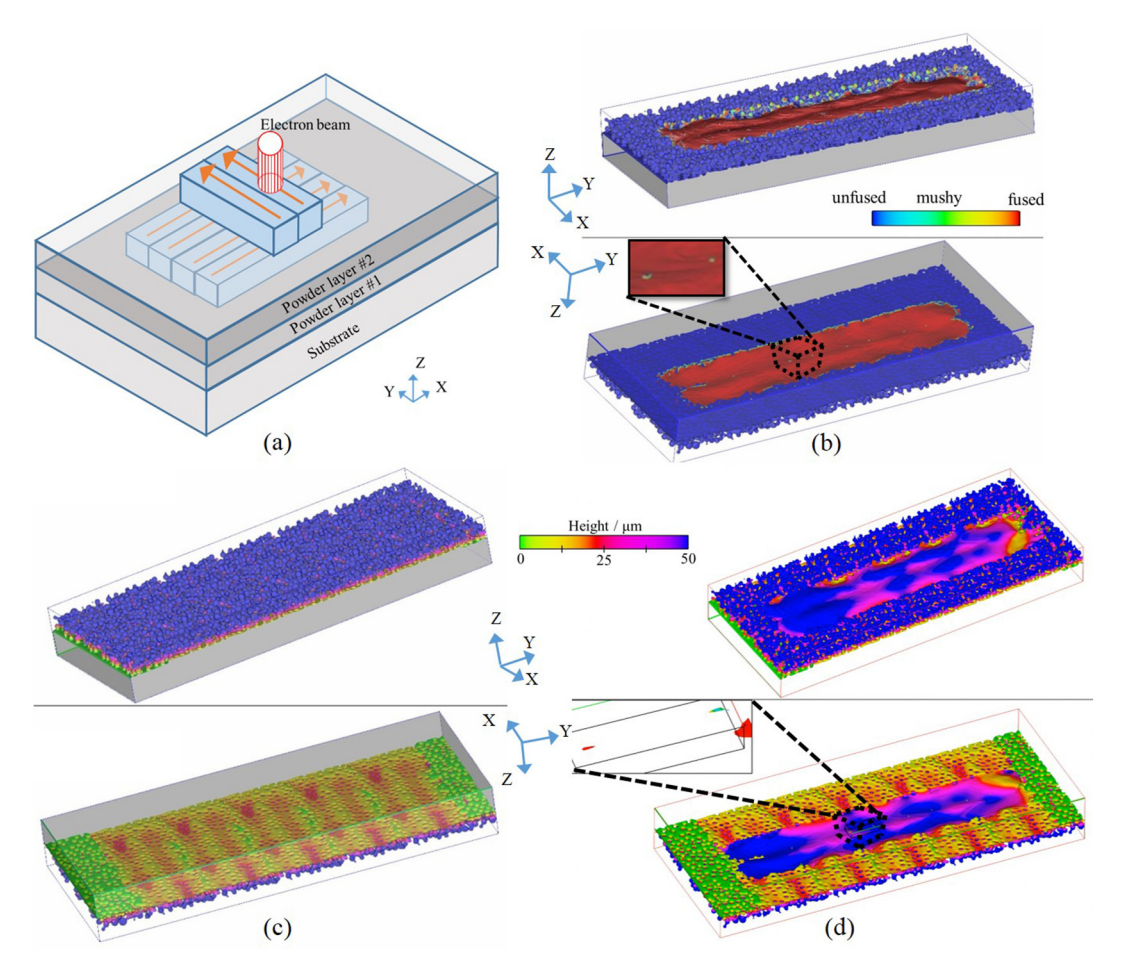


Fig. 8. Layer-wise rotated for 90° . (a) Schematic. (b) 3D view of simulation result colored by fusion. (c) 3D view of free surfaces colored by height before melting the second powder layer, and the scan direction in the first layer is shown to be along x axis (perpendicular to the scan direction in the second layer). (d) 3D view of free surfaces after melting the second layer. Zoomed insets in (b) and (d) highlight void formation. In (b), (c) and (d), the upper sub-figures are viewed from above (the +z direction), and the lower ones are viewed from below (the -z direction).

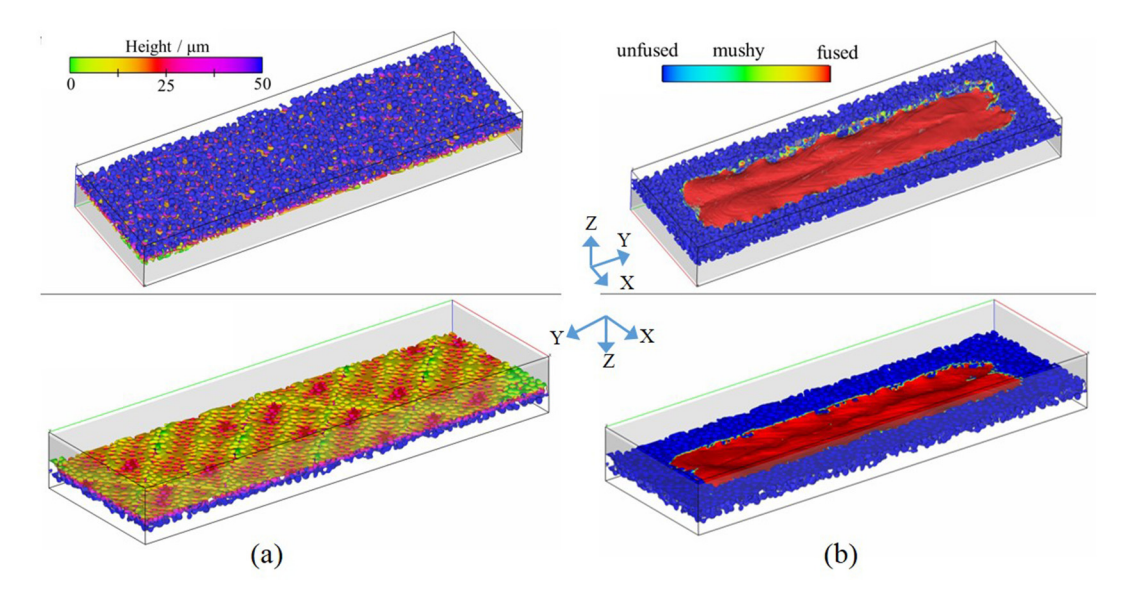


Fig. 9. Layer-wise rotated by 45°: (a) 3D view of free surfaces colored by height, before melting the second powder layer, where the scan direction in the first layer is 45° from y axis (the scan direction in the second powder layer); (b) 3D view of free surfaces colored by fusion, after melting the second layer. The upper sub-figures show views from above (the +z direction), and the lower ones show views from below (the -z direction).

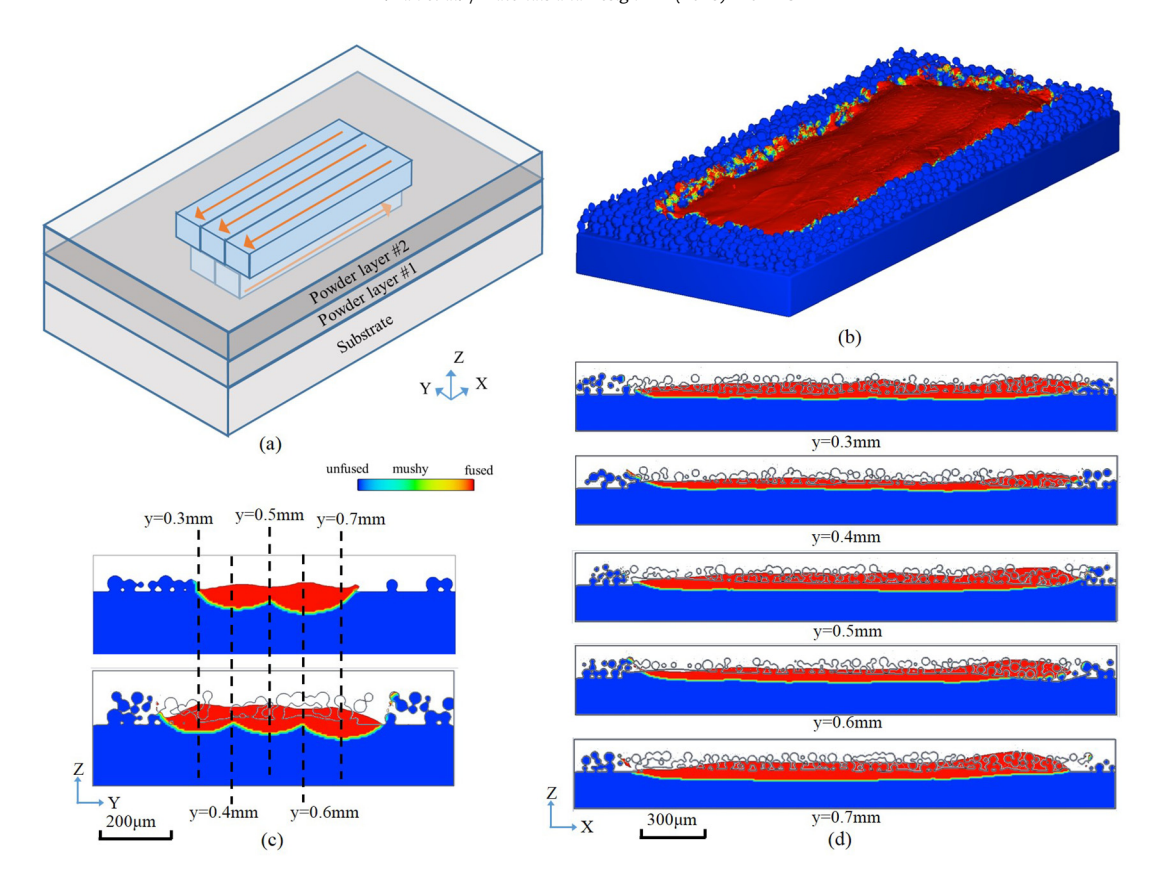


Fig. 10. Layer-wise interlaced scan strategy: (a) Schematic, (b) 3D view of simulation result, (c) YZ cross section view at the middle, the upper one is after melting the two tracks in the first layer and the other below is after melting the three tracks in the second layer, (d) XZ cross section view at various locations, and no voids are observed. In (c) and (d), the outlines represent the configuration of the first layer fused zone and the powder particles before scanning the second layer.

and experiments. It remains a challenging problem to explicitly incorporate the gas phase in the model. Nevertheless, the prediction of these lack-of-fusion voids is valuable, since it can provide clear guidance for parameter selection (power, hatching distance, etc.) to avoid these voids, and gives insights into anomalous effects near track start and end locations and at interfaces between multiple tracks and layers, as described in this work.

5. Conclusion

We propose an integrate modeling framework consisting of a DEM model of powder spreading and a thermal-fluid flow model of powder melting, in which 3D geometrical data is exchanged. This approach is able to link the process details to the resulting material structure. More importantly, this approach enables us to perform 3D simulations of the manufacturing process of multiple tracks and multiple layers using various layer-wise scan strategies. The primary conclusions are as follows:

- Both inter-track and inter-layer voids are highly likely to be generated in the edge regions of the part. The contouring scan strategy is an effective way to eliminate these voids.
- Considering the densification of the powder bed and height fluctuation of dense tracks, the optimal fabrication parameters should ensure sufficient fusion of a powder layer of more than twice the designated layer thickness.
- The layer-wise interlace scan strategy is more beneficial for reducing the porosity in as-built products, while in layer-wise rotated scan strategies, voids are most likely to be observed in the central spots between scan paths.

The simulation results are qualitatively validated by experimental observations. The void size is mainly determined by the size distribution of powder and the process parameters (including hatch spacing, layer thickness, power and speed).

By integrating the powder spreading model with the powder melting model, we are able to determine the impact of various process parameters on part quality. This provides valuable insights on the design and optimization of additive manufacturing systems. Future improvements in the efficiency of computational method are expected to further enhance the usefulness of this integrated computational approach in process design. Until then, systematic investigations of surface roughness and complex structures can be performed by simulating the manufacturing process of tens or even hundreds of layers and tracks.

Acknowledgments

G. J. Wagner and W. Liu acknowledge the support by the National Science Foundation (NSF) Cyber-Physical Systems (CPS) under grant No. CPS/CMMI-1646592. W. Liu and W. Yan acknowledge the support by Center for Hierarchical Materials Design (CHiMaD) under grant No. 70NANB14H012. S. Lin acknowledges the support by the NSF Graduate Research Fellowship under Grant No. DGE-1324585.

References

- W. Ge, F. Lin, C. Guo, Microstructure and mechanical property of electron beam selective melting Ti-6Al-4V/Ti-Al structural gradient material, 26th Annual International Symposium on Solid Freeform Fabrication, Austin, Texas, 2015,
- [2] W. Ge, C. Guo, F. Lin, Microstructures of components synthesized via electron beam selective melting using blended pre-alloyed powders of Ti-6Al-4V and Ti-45Al-7Nb, Rare Metal Mater. Eng. 44 (2015) 2623–2627.

- [3] C. Guo, W. Ge, F. Lin, Dual-material electron beam selective melting: hardware development and validation studies, Engineering 1 (1) (2015) 124.
- [4] J. Smith, W. Xiong, W. Yan, S. Lin, P. Cheng, O.L. Kafka, G.J. Wagner, J. Cao, W.K. Liu, Linking process, structure, property, and performance for metal-based additive manufacturing: computational approaches with experimental support, Comput. Mech. 57 (2016) 583–610.
- [5] I. Yadroitsev, A. Gusarov, I. Yadroitsava, I. Smurov, Single track formation in selective laser melting of metal powders, J. Mater. Process. Technol. 210 (12) (2010) 1624–1631.
- [6] C. Körner, A. Bauereiß, E. Attar, Fundamental consolidation mechanisms during selective beam melting of powders, Model. Simul. Mater. Sci. Eng. 21 (8) (2013) 085011.
- [7] T. Wohler, Additive Manufacturing and 3D Printing-State of the Industry Annual Worldwide Progress Report 2015, Wohler's Associates, Inc, Fort Collins, CO. 2015.
- [8] C. Körner, E. Attar, P. Heinl, Mesoscopic simulation of selective beam melting processes, J. Mater. Process. Technol. 211 (6) (2011) 978–987.
- [9] S.A. Khairallah, A.T. Anderson, A. Rubenchik, W.E. King, Laser powder-bed fusion additive manufacturing: physics of complex melt flow and formation mechanisms of pores, spatter, and denudation zones, Acta Mater. 108 (2016) 26.45
- [10] W. King, A. Anderson, R. Ferencz, N. Hodge, C. Kamath, S. Khairallah, Overview of modelling and simulation of metal powder bed fusion process at Lawrence Livermore National Laboratory, Mater. Sci. Technol. 31 (8) (2015) 957–968.
- [11] A. Klassen, V.E. Forster, V. Juechter, C. Körner, Numerical simulation of multi-component evaporation during selective electron beam melting of TiAl, J. Mater. Process. Technol. 247 (2017) 280–288.
- [12] R. Ammer, M. Markl, U. Ljungblad, C. Körner, U. Rüde, Simulating fast electron beam melting with a parallel thermal free surface lattice Boltzmann method, Comput. Math. Appl. 67 (2) (2014) 318–330.
- [13] C. Qiu, C. Panwisawas, M. Ward, H.C. Basoalto, J.W. Brooks, M.M. Attallah, On the role of melt flow into the surface structure and porosity development during selective laser melting, Acta Mater. 96 (2015) 72–79.
- [14] T.I. Zohdi, Rapid simulation of laser processing of discrete particulate materials, Arch. Comput. Methods Eng. 20 (4) (2013) 309–325.
- [15] T. Zohdi, A direct particle-based computational framework for electrically enhanced thermo-mechanical sintering of powdered materials, Mathe. Mech. Solids 19 (1) (2014) 93–113.
- [16] J.C. Steuben, A.P. Iliopoulos, J.G. Michopoulos, On multiphysics discrete element modeling of powder-based additive manufacturing processes, ASME 2016 International Design Engineering Technical Conferences and Computers and Information in Engineering Conference, American Society of Mechanical Engineers, 2016, pp. V01AT02A032.

- [17] J.C. Steuben, A.P. Iliopoulos, J.G. Michopoulos, Discrete element modeling of particle-based additive manufacturing processes, Comput. Methods Appl. Mech. Eng. 305 (2016) 537–561.
- [18] E.J. Parteli, DEM simulation of particles of complex shapes using the multisphere method: application for additive manufacturing, AIP Conference Proceedings, vol. 1542, AIP. 2013, pp. 185–188.
- [19] Z. Xiang, M. Yin, Z. Deng, X. Mei, G. Yin, Simulation of forming process of powder bed for additive manufacturing, J. Manuf. Sci. Eng. 138 (8) (2016) 081002.
- [20] E.J. Parteli, T. Pöschel, Particle-based simulation of powder application in additive manufacturing, Powder Technol. 288 (2016) 96–102.
- [21] T. Scharowsky, F. Osmanlic, R. Singer, C. Körner, Melt pool dynamics during selective electron beam melting, Appl. Phys. A 114 (4) (2014) 1303–1307.
- [22] W. Yan, W. Ge, Y. Qian, S. Lin, B. Zhou, W.K. Liu, F. Lin, G.J. Wagner, Multiphysics modeling of single/multiple-track defect mechanisms in electron beam selective melting, Acta Mater. 134 (2017) 324–333.
- [23] T. Theofanous, L. Biasi, H. Isbin, H. Fauske, A theoretical study on bubble growth in constant and time-dependent pressure fields, Chem. Eng. Sci. 24 (5) (1969) 885–897.
- [24] W. Yan, J. Smith, W. Ge, F. Lin, W.K. Liu, Multiscale modeling of electron beam and substrate interaction: a new heat source model, Comput. Mech. 56 (2) (2015) 265–276.
- [25] W. Yan, W. Ge, J. Smith, S. Lin, O.L. Kafka, F. Lin, W.K. Liu, Multi-s-cale modeling of electron beam melting of functionally graded materials, Acta Mater. 115 (2016) 403–412.
- [26] J. Milberg, M. Sigl, Electron beam sintering of metal powder, Prod. Eng. 2 (2) (2008) 117–122.
- [27] C. Hirt, B. Nichols, Flow-3D User's manual.
- [28] C. Guo, W. Ge, F. Lin, Effects of scanning parameters on material deposition during electron beam selective melting of Ti-6Al-4V powder, J. Mater. Process. Technol. 217 (2015) 148–157.
- [29] P. Frigola, O. Harrysson, T. Horn, H. West, R. Aman, M. Rigsbee, D. Ramirez, L. Murr, F. Medina, R. Wicker, E. Rodriguez, Fabricating copper components with electron beam melting, Adv. Mater. Process. (2014) 20–24.
- [30] S. Tammas-Williams, H. Zhao, F. Léonard, F. Derguti, I. Todd, P. Prangnell, XCT Analysis of the influence of melt strategies on defect population in Ti-6Al-4V components manufactured by selective electron beam melting, Mater. Charact. 102 (2015) 47–61.
- [31] D. Wang, C. Yu, J. Ma, W. Liu, Z. Shen, Densification and crack suppression in selective laser melting of pure molybdenum, Mater. Des. 129 (2017) 44–52.
- [32] W.E. King, H.D. Barth, V.M. Castillo, G.F. Gallegos, J.W. Gibbs, D.E. Hahn, C. Kamath, A.M. Rubenchik, Observation of keyhole-mode laser melting in laser powder-bed fusion additive manufacturing, J. Mater. Process. Technol. 214 (12) (2014) 2915–2925.